aerospace

MDPI

Article

Rigid–Flexible Coupling Dynamics Analysis of Coordination Arm and Application of a New Directional Subinterval Uncertainty Analysis Method

Xuan Gao, Longmiao Chen * and Jingsong Tang

School of Mechanical Engineering, Nanjing University of Science and Technology, Nanjing 210094, China; gaoxuan@njust.edu.cn (X.G.); tangjs@njust.edu.cn (J.T.)
* Correspondence: chenlongmiao@njust.edu.cn

Abstract: Cartridge delivery systems are commonly employed in aerospace engineering for the transportation of cylindrical projectiles. The coordination mechanism plays a pivotal role in ensuring reliable cartridge conveying, with its positioning accuracy being of utmost importance. However, accurately depicting the nonlinear relationship between input parameters and output response is challenging due to the involvement of numerous complex, uncertain factors during the movement process of the coordination mechanism. To address this issue, this study proposes a dynamics model that incorporates hinged gaps to represent rigid–flexible coupling within the coordination mechanism. Experimental validation confirms its effectiveness, while computational efficiency is enhanced through the utilization of a deep learning neural network surrogate model. Furthermore, an improved method for the uncertainty analysis of directional subintervals is introduced and applied to analyze uncertainty in coordination mechanisms, yielding results that demonstrate superior efficiency compared to other approaches.

Keywords: coordinating arm; rigid–flexible coupling; agent model; uncertainty analysis; directional subinterval prediction

Citation: Gao, X.; Chen, L.; Tang, J. Rigid–Flexible Coupling Dynamics Analysis of Coordination Arm and Application of a New Directional Subinterval Uncertainty Analysis Method. *Aerospace* **2024**, *11*, 419. https://doi.org/10.3390/aerospace11060419

Academic Editor: Chen Jiang

Received: 28 March 2024
Revised: 10 May 2024
Accepted: 20 May 2024
Published: 22 May 2024

1. Introduction

Cartridge delivery systems are often used in aerospace engineering to transport cylindrical projectiles. The coordination mechanism is a crucial component of a cartridge conveying system, primarily responsible for receiving paper cartridges from external sources, storing and aligning them to the desired angle, and subsequently propelling them into the pipeline. Its primary function involves the reciprocating movement of the load between the drug receiving position and drug delivery position. In addition to ensuring its normal operation, it must also possess the ability to swiftly and accurately coordinate in place while maintaining a lightweight design under high loads. Based on actual test records, various uncertain factors, such as flexible vibrations within the mechanism and clearances between components, can significantly impact the stability and reliability of the coordination mechanism. Therefore, conducting an uncertainty analysis of this coordination mechanism holds immense significance in advancing research on cartridge conveying systems.

There are various quantitative analysis methods for uncertainty in mechanism dynamics systems. The central idea behind these methods is to clarify different sources of uncertainty in order to fully capture the stochastic behavior of dynamics systems so as to quantify the uncertainty consequences through numerical or experimental methods [1]. At present, mainstream uncertainty propagation methods mainly include Monte Carlo simulation (MCS), the local expansion method, the orthogonal function expansion method, the numerical integration method, etc. The Monte Carlo method is also known as the random sampling method or statistical test method. With an increase in simulation times,

its calculation results will gradually approach an accurate solution. Thanks to the development of computer technology, the Monte Carlo simulation method has been widely used in many engineering fields, and it is usually used as a quasi-accurate calculation method to verify the accuracy of other approximate methods [2]. However, as this method requires a large number of simulation tests to ensure the accuracy of the calculation results, it has low calculation efficiency and high calculation costs, which make it difficult to apply to many practical engineering problems, especially complex large-scale problems. By improving sampling technology, several variants of the direct Monte Carlo method, such as the important sampling method [3,4], the subset simulation method [5–7], and the direction sampling method [8], have been proposed and developed, which can greatly improve the solving efficiency of the Monte Carlo method under certain conditions.

The above methods were all developed based on probability theory. There are two main problems in applying probabilistic methods to uncertainty analysis. First, obtaining an accurate trend of the probability distribution of uncertain variables depends on an extensive statistical analysis of a large number of test samples. This method involves huge computational complexity and may not be feasible or cost-effective for many practical engineering problems. Second, because it is difficult to obtain accurate parameter distributions, subjective assumptions are often made when using probabilistic methods for uncertainty analysis. However, even if there is only a small deviation in the parameter distribution, the results of an uncertainty analysis will produce significant errors [9]. Non-probabilistic methods can effectively solve these shortcomings. Non-probabilistic models do not require a detailed understanding of the sample characteristics of uncertain variables but focus on determining the size or boundary of variable uncertainty, which is relatively easy. Second, even if the data are limited, the size or upper and lower boundaries of variable uncertainty can be more accurately determined, thus improving the accuracy of uncertainty analysis.

Since the middle and late 1980s, in order to overcome the dependence of classical probability methods on large sample sizes, the interval model has been introduced into the field of structural engineering to describe the fluctuation range of uncertain parameters. In the classical interval model [10], a single uncertain parameter is described as a fluctuation-bounded interval variable, while the uncertain domain of multiple independent parameters constitutes a "multi-dimensional box". At present, in the uncertain analysis problem, commonly used interval analysis methods can be divided into the vertex method (VM) [11,12], the configuration method [13–16], the Taylor expansion method [17–19], etc. The vertex method assumes that the structural response obtains its response boundary at the vertex of the uncertain domain. However, the calculation speed of the vertex method increases exponentially with an increase in the interval parameters, which is unacceptable for large structures. The configuration method constructs a reasonable surrogate model by setting a certain number of sample points in the uncertain parameter space so as to obtain a range of structural responses. In order to meet certain accuracy requirements, a large number of sample points are usually required. Especially when there are many interval parameters, the calculation cost increases exponentially and then gets into a dimension disaster. The Taylor expansion method is used to solve the uncertain static response problem. This method involves carrying out the first- or second-order Taylor series expansion of the structural response function at the midpoint of the interval to obtain the value range or interval boundary of the structural response. The biggest advantage of this method is that it has high solving efficiency, and the calculation cost increases linearly with an increase in the interval parameters. The Taylor expansion method only considers the lower-order terms of the Taylor series expansion, ignoring the higher-order terms. When the interval parameters are largely uncertain, it is difficult to use the first-order Taylor expansion method to obtain high-precision response results, and it even leads to a distortion of the results due to linear approximation [20].

For the interval analysis problem with a high degree of uncertainty or nonlinearity, Qiu and Elishakoff [21] proposed a subinterval prediction method, which divided the original interval difference into several continuous subintervals, performed an interval analysis on

these subintervals, respectively, and finally combined the interval analysis results. Zhou et al. [22] used the subinterval prediction method to solve the structural analysis problem with large uncertain parameters. Chen et al. [23] proposed a subinterval homogenization method to identify the elasticity characteristics of periodic microstructure problems with interval uncertainty and compared the results obtained with the MCS method to verify the accuracy of the method. Fu et al. [24] proposed a dimension reduction subinterval prediction method to combine the dimension reduction method and the subinterval prediction method to deal with strong nonlinear and high-dimensional problems. The subinterval prediction method has good calculation accuracy, but there are still problems in determining the number of subintervals and calculation efficiency, especially for high-dimensional problems, in which the subinterval prediction method will produce a "dimensionality explosion", resulting in low calculation efficiency.

The proxy model is a response function approximation constructed through an experimental design which serves as an approximate technique for addressing multivariable problems. It significantly enhances computational efficiency while ensuring the fitting accuracy of the proxy model and can be easily integrated with other methods, making it widely employed in the field of engineering design at present. Currently, commonly used proxy models primarily encompass machine learning [25,26] and deep learning neural network models. Among them, the deep learning neural network model consists of multiple hidden layers and exhibits exceptional fitting capability for complex, nonlinear relationships. Henceforth, this paper employs the DNN proxy model as a substitute for the high-precision dynamic model for simulation calculations in order to reduce computational costs.

The present paper establishes a rigid–flexible coupling dynamics model of the articulated gap to investigate the coordination mechanism of an ammunition automatic loading system. Experimental tests are conducted to validate the accuracy and effectiveness of this dynamics model. Subsequently, in order to reduce computational complexity during the uncertainty analysis of the coordination mechanism, a deep neural network surrogate model is employed for simulation calculations as a substitute for the high-precision dynamics model. Furthermore, building upon the classical subinterval prediction method based on Taylor expansion, we propose an improved directional subinterval prediction approach that incorporates gradient information within specific intervals. An adaptive convergence method is also designed to enhance calculation efficiency. Finally, we apply this methodology to analyze positioning accuracy uncertainties in the coordination mechanism and compare it with Monte Carlo simulations (MCSs) and other analysis methods, demonstrating its superior efficiency and accuracy.

2. Dynamics Modeling of Coordinating Mechanism

A schematic diagram of the coordination mechanism structure of the coordination drug delivery device is shown in Figure 1 below. The coordination mechanism is driven by a hydraulic cylinder to rotate around the lug shaft, enabling the coordination function of the flipping and drug delivery mechanisms at various angles of attack. This complex and irregular mechanical structure primarily consists of rectangular tubular trusses welded together. Prior to dynamic modeling, it is necessary to simplify its structure and make reasonable assumptions. The rotary wheel hub serves as a pivotal component attached to the lug shaft, connected through high-precision bearings. For dynamic modeling purposes, it can be treated as a rigid body while disregarding any gaps between the lug shafts. The flexible coordination arm acts as the main load-bearing component, linked to the flipping mechanism via a rigid spline shaft and initially secured in position with pre-pressure. The drug delivery mechanism and flipping mechanism are firmly connected using bolts without any movement during coordination; thus, they can be simplified as concentrated masses affixed at the end of the flexible coordination arm. Pin shafts hinge both the upper fulcrums of the coordination cylinder and the flexible coordination arm, which are further connected to the drug delivery device frame through fixed pin shafts. Considering that

uncertainties in processing technology may result in unavoidable hinge gaps, these gaps need thorough consideration during dynamics modeling.

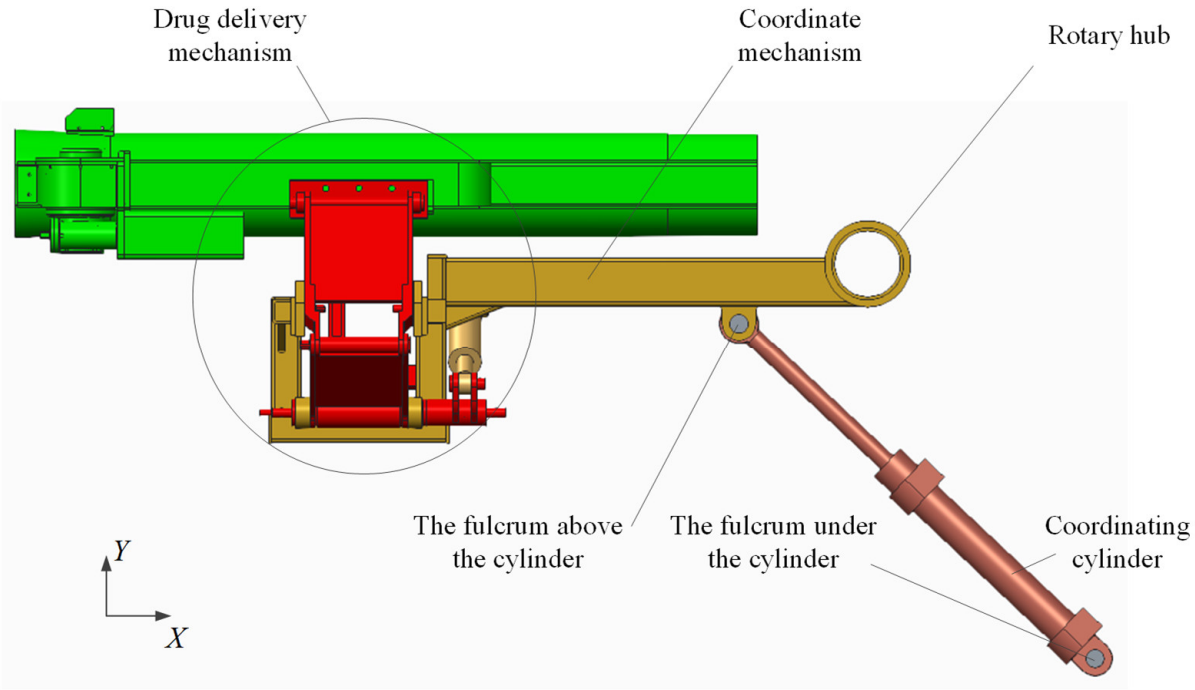

Figure 1. Schematic diagram of coordination mechanism.

2.1. Mathematical Model of Flexible Cantilever Beam

According to the schematic diagram of the coordination mechanism in Figure 1, the rigid–flexible coupling system of the coordination mechanism constitutes a typical class I rigid–flexible coupling problem [27], in which the coordination arm can be regarded as a flexible cantilever beam, and the overturning and dosing mechanisms can be regarded as fixed loads. Based on this, the dynamic modeling of the coordination arm is conducted, and its deformation model is shown in Figure 2. The coordinate system encompasses the inertial coordinate system, $O - XY$, and the floating coordinate system, $o - xy$, established based on the flexible beam.

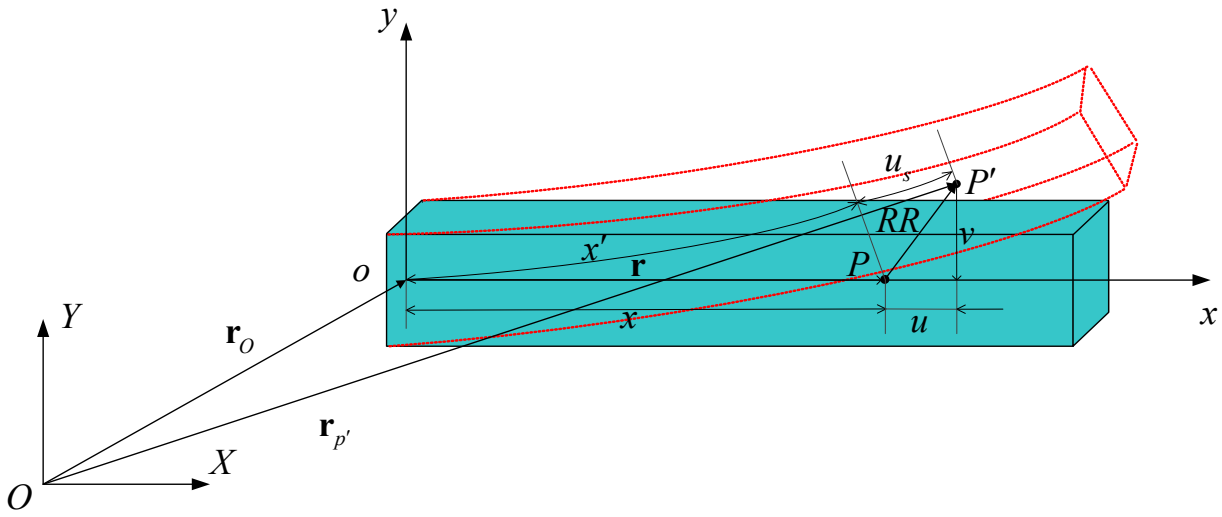

Figure 2. Deformation of flexible cantilever beam.

It can be seen from Figure 2 that the vector of the origin of the floating coordinate system with respect to the inertial coordinate system is $\mathbf{r}_O$. Take any point, P, on the flexible cantilever beam; its vector in the floating coordinate system before deformation is $\mathbf{r}$, and its coordinates in the floating coordinate system are $[x, 0]^{\mathbf{T}}$. After the deformation of the flexible cantilever beam, the point reaches point P', and then the vector of point P' with respect to the inertial coordinate system can be expressed as follows:

$$\mathbf{r}_{p'} = \mathbf{r}_O + \mathbf{C}(\mathbf{r} + RR), \tag{1}$$

where $\mathbf{C}$ is the coordinate transformation matrix of the floating coordinate system relative to the inertial coordinate system, RR is the deformation displacement vector from point P to point P' before and after deformation, and its coordinates in the floating coordinate system are as follows:

$$\mathbf{r}_u = \begin{bmatrix} u(x,t) \\ v(x,t) \end{bmatrix} = \begin{bmatrix} w_1(x,t) + w_c(x,t) \\ w_2(x,t) \end{bmatrix} = \begin{bmatrix} w_1(x,t) - \frac{1}{2}\int_0^x \left(\frac{\partial w_2(\varepsilon,t)}{\partial \varepsilon}\right)^2 d\varepsilon \\ w_2(x,t) \end{bmatrix}, \tag{2}$$

where $w_1(x,t)$ is the x-axis directional extension in the floating coordinate system, $w_2(x,t)$ is the lateral bending deformation, and $w_c(x,t) = -\frac{1}{2}\int_0^x \left(\frac{\partial w_2(\varepsilon,t)}{\partial \varepsilon}\right)^2 d\varepsilon$ is the longitudinal deformation caused by the bending deformation of the flexible cantilever beam, which is called the nonlinear coupling deformation [1]. When the flexible cantilever beam works at a relatively high speed, the influence of u_c on its dynamic characteristics cannot be ignored.

The finite element method and the hypothetical mode method are usually adopted to solve the vibration model of a flexible cantilever beam. Because the dynamics model established by the finite element method has many degrees of freedom, which is not conducive to active control design, the structural control of the whole system is actually realized by controlling several major modes. Therefore, the discretization method of the hypothetical mode method is more convenient for subsequent control research to establish the dynamics model. The specific expression for the deformation of the flexible cantilever beam is as follows:

$$\begin{cases} w_1(x,t) = \mathbf{N}_1(x)\mathbf{q}_1(t) \\ w_2(x,t) = \mathbf{N}_2(x)\mathbf{q}_2(t) \end{cases}, \tag{3}$$

where $\mathbf{N}_1(x)$ and $\mathbf{N}_2(x)$ are, respectively, the eigenfunction row vectors of longitudinal and transverse vibrations and $\mathbf{q}_1(t)$ and $\mathbf{q}_2(t)$ are, respectively, the eigenfunction column vectors of longitudinal and transverse vibrations, which can be expressed as follows:

$$\begin{cases} \mathbf{N}_i(x) = (N_1^{(i)}(x), N_2^{(i)}(x), \cdots N_n^{(i)}(x)) \\ \mathbf{q}_i = (q_1^{(i)}, q_2^{(i)}, \cdots q_n^{(i)})^{\mathrm{T}} \end{cases}, \tag{4}$$

where, for $i = 1, 2$, n is the number of hypothetical modes. The eigenfunction can be expressed as follows:

$$\begin{aligned} &N_n^{(1)}(x) = \sin\tfrac{(2j-1)}{2L}x,\ j = 1, 2 \cdots n \\ &N_n^{(2)}(x) = \cos\beta_j x - \cosh\beta_j x + \gamma_j(\sin\beta_j x - \sinh\beta_j x),\ j = 1, 2 \cdots n \\ &\gamma_i = \tfrac{(\cos\beta_i x + \cosh\beta_i x)}{(\sin\beta_i x + \sinh\beta_i x)} \end{aligned} \tag{5}$$

Then, the deformation displacement vector, RR, from point P to point P' before and after deformation can be expressed as follows:

$$RR = \begin{bmatrix} w_1 - \frac{1}{2}\int_0^x \left(\frac{\partial w_2(\varepsilon,t)}{\partial \varepsilon}\right)^2 d\varepsilon \\ w_2 \end{bmatrix} = \begin{bmatrix} \mathbf{N}_1(x)\mathbf{q}_1(t) - \frac{1}{2}\mathbf{q}_2^{\mathrm{T}}\mathbf{S}(x)\mathbf{q}_2(t) \\ \mathbf{N}_2(x)\mathbf{q}_2(t) \end{bmatrix} \tag{6}$$

In summary, the generalized coordinates of a flexible cantilever beam can be expressed as follows:

$$\mathbf{Q}_f = \left[\mathbf{r}_O, \theta, \mathbf{q}_1^{\mathrm{T}}, \mathbf{q}_2^{\mathrm{T}}\right]^{\mathrm{T}}, \tag{7}$$

where $\mathbf{r}_O$ and θ are the reference coordinates of the floating coordinate system. According to the second type of Lagrange equations, the rigid–flexible coupling dynamic equation of the flexible cantilever beam can be derived as follows:

$$\mathbf{M}\ddot{\mathbf{Q}}_f + \mathbf{C}\dot{\mathbf{Q}}_f + \mathbf{K}\mathbf{Q}_f = \mathbf{F}, \tag{8}$$

where $\mathbf{M}$ is the generalized mass matrix, $\mathbf{C}$ is the generalized damping matrix, $\mathbf{K}$ is the generalized stiffness matrix, and $\mathbf{F}$ is the generalized force matrix.

2.2. Mathematical Model of Contact Force in Clearance of Shaft–Hole Joint

When the two bodies represented by the shaft and hub undergo a curved surface contact collision, the contact collision force, $\mathbf{F}_C$, can be expressed by the combined force of the normal contact force, $\mathbf{F}_N$, and the tangential contact force, $\mathbf{F}_T$:

$$\mathbf{F}_C = \mathbf{F}_N + \mathbf{F}_T \tag{9}$$

In the classical dynamic modeling of contact collision force, the Hertz contact model is usually used to represent the contact of shaft–hole articulated clearance, but this model assumes that the contact collision between the shaft and the hub is completely elastic, ignoring the energy loss in the process. However, in practical engineering problems, more factors should be considered in the contact collision force, such as the relative contact velocity, the geometric parameters of the shaft and hub, material properties, etc. In this paper, a mixed contact force model is adopted to construct the normal contact collision force of shaft–hole articulated clearance [27], which can be expressed as follows:

$$F_N = K_n\delta^n + D_{mod}\dot{\delta}, \tag{10}$$

where $D_{mod} = \frac{3K_n(1-c_r^2)e^{2(1-c_r)}\delta^n}{4\dot{\delta}^-}$ is the improved nonlinear damping coefficient. $K_n = \frac{1}{8}\pi E^*\sqrt{\frac{2\delta(3(R_h-R_a)+2\delta)^2}{(R_h-R_a+\delta)^3}}$ is the improved nonlinear stiffness coefficient in the mixed contact force model, where $E^* = \frac{E_a(1-v_h^2)+E_h(1-v_a^2)}{E_hE_a}$ is the composite elastic modulus, E_a and E_h are the elastic moduli of the shaft and hub, v_a and v_h are the Poisson's ratios of the shaft and hub, δ is the initial collision velocity, c_r is the recovery coefficient, and n is the exponential coefficient.

The tangential contact force of shaft–hole articulated clearance is usually replaced by a tangential friction force. In this paper, the Ambrosio coulomb friction model is adopted, which is a continuous function of the tangential relative velocity and can guarantee the stability and continuity of numerical integration [27]. Its expression form is shown as follows:

$$F_T = -f_k c_d F_N \mathrm{sgn}(V_t), \tag{11}$$

where f_k is the friction coefficient and c_d is the dynamic correction coefficient related to tangential velocity, which can be expressed as follows:

$$c_d = \begin{cases} 0 & V_t \le v_0 \\ \frac{V_t - v_0}{v_1 - v_0} & v_0 \le V_t \le v_1 \\ 1 & V_t \ge v_1 \end{cases}, \quad (12)$$

where v_0 and v_1 are the boundary values of the given tangential velocity interval.

2.3. Experimental Study and Model Verification of Coordination Mechanism

In order to verify the accuracy and effectiveness of the dynamics model of the coordinating mechanism, this section will conduct a comparative verification of the dynamics model based on a principle prototype platform built in the laboratory. The principle prototype platform is shown in Figure 3. The test process of the coordination mechanism is simplified as follows: the hydraulic oil source provides power to the coordination driving cylinder, while the PLC control box regulates the opening degree of the hydraulic servo valve based on instructions, thereby enabling the completion of coordinated actions by driving the coordination cylinder. During this process, pressure sensors installed on the coordination driving cylinder measure and record data regarding both rodless cavity and rod cavity pressures. These measured values serve as inputs for a dynamic simulation model of the coordination mechanism. Additionally, an angle encoder is positioned at the hinge connecting the coordination arm and ear shaft to monitor real-time changes in angle relative to their initial positions. This information serves as output for evaluating the actual conditions within the coordination mechanism. All aforementioned data are recorded in real time using a data acquisition instrument for subsequent model comparison and verification.

This paper mainly conducts tests and records for the condition that the coordination mechanism is fully charged and the coordination arm is coordinated from the 3° drug contact position on the horizontal surface to the 60° angle position below the horizontal surface, namely a complete coordination angle of 63°. As shown in Figures 4–6 below, Figures 4 and 5 are the pressure smooth curves of the rodless cavity and the rod-loaded cavity of the coordination driving cylinder measured by the pressure sensor in real time during the coordination mechanism's coordination to the 60° angle action, respectively, and Figure 6 is the cylinder force curve obtained by converting the pressure data of the rodless cavity and the rod-loaded cavity of the coordination driving cylinder.

In order to verify the validity of the dynamics simulation model, Test Data 1 were selected as the dynamic input into the dynamics simulation model of the coordinating mechanism, and the angular displacement of the coordinating mechanism coordinated to a 60° incident angle under the full charge state was compared with the real-time measured results of the angle encoder when the coordinating mechanism was coordinated to a 60° incident angle under the actual working conditions, as shown in Figure 7. Through comparative analysis, the simulation results were found to be close to the test results, indicating the rationality and validity of the dynamics simulation model of the coordinating mechanism, and it can be considered that the simulation model can be applied to the subsequent dynamics characteristic analysis, uncertainty analysis, and optimization.

Figure 3. Principle prototype platform composition diagram.

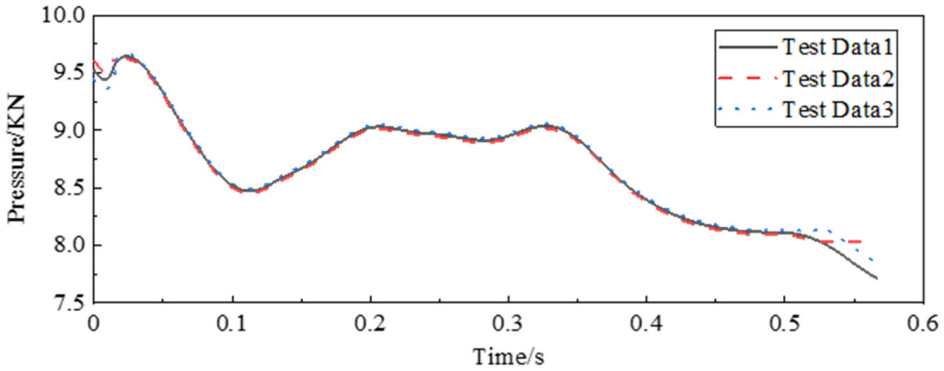

Figure 4. Coordination cylinder's rodless chamber pressure test data curve.

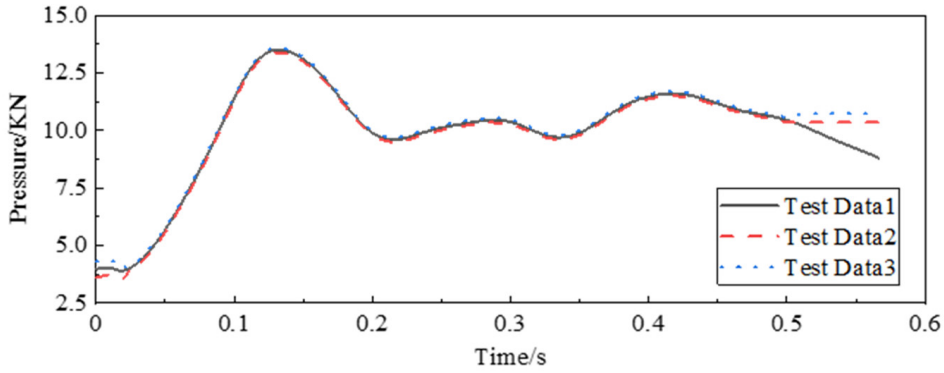

Figure 5. Coordinated cylinder's pressure test data curve with rod cavity.

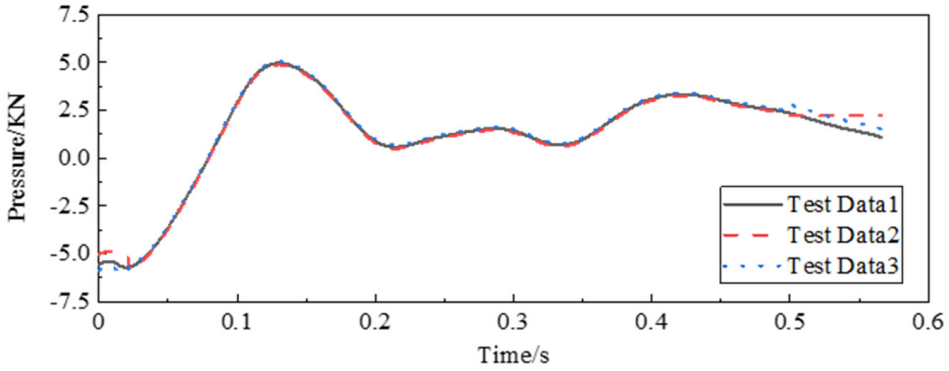

Figure 6. Coordinated cylinder's resultant pressure test data curve.

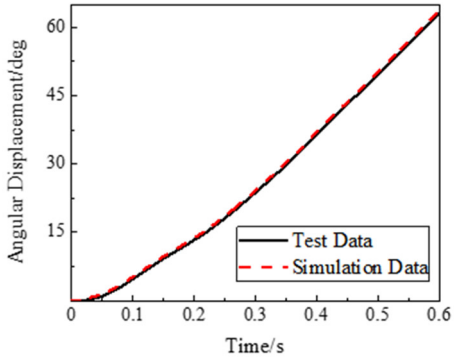

Figure 7. Comparison of angular displacement test data and simulation data of coordinate mechanism.

3. Construction of Coordination Agency Agent Model

The structure of the ammunition automatic loading system is complex and has obvious structural characteristics. The structural dynamics model takes into account a variety of factors, resulting in a strong nonlinear relationship between input and output. In the process of the uncertainty analysis and optimization of the coordination mechanism, the dynamics model needs to be called upon for calculation many times. With an improvement in the accuracy of the dynamics model, the cost of a single calculation increases significantly. Directly calling upon the original dynamics model will lead to unbearable calculation costs. Therefore, it is a common solution to use a high-precision surrogate model instead of the dynamics simulation model. The main advantage of the surrogate model method is the ability to use an implicit approximation function to approximately replace the original dynamics model so as to carry out calculation analysis or optimization and reduce

calculation costs. In this section, a surrogate model of the coordination mechanism is constructed based on a deep neural network (DNN).

3.1. Deep Neural Network Architecture

The neural network method is widely used in surrogate model research due to its excellent nonlinear fitting ability. It is usually composed of a multilayer system, consisting of an input layer, an output layer, and a hidden layer, which can transform input information into useful output information. In research on multi-hidden neural network algorithms, many scholars have found that with an increase in the number of hidden layers, the ability of neural network models to analyze complex patterns is also improved. Multi-hidden neural networks are actually deep versions of shallow neural networks which attempt to express features by using more neurons, which is typical of deep neural networks (DNNs). Compared with the classical structure of artificial neural network models, the main difference between these and DNNs is that they have more hidden layers. As long as there are more than three hidden layers, it can be defined as a DNN, and its basic architecture is shown in Figure 8. DNNs can be described as having a layout consisting of multilayer neurons, which are interconnected by weights and adjusted iteratively through an optimization process. The initial data are input into the input layer, and then the input layer distributes the data to each neuron in the first hidden layer. The output of the first hidden layer is then passed to the next hidden layer until it reaches the output layer, where data are distributed to the output neurons, which are equal in number to the number of categories. During training, the DNN uses a backpropagation algorithm. It compares the network output with the expected output to calculate the error and propagates the error back. The random gradient descent method, combined with a loss function, is used to update the weights. This process is iterated and repeated, updating all training data on the entire network in a training round. The single-neuron model of a DNN is shown in Figure 9.

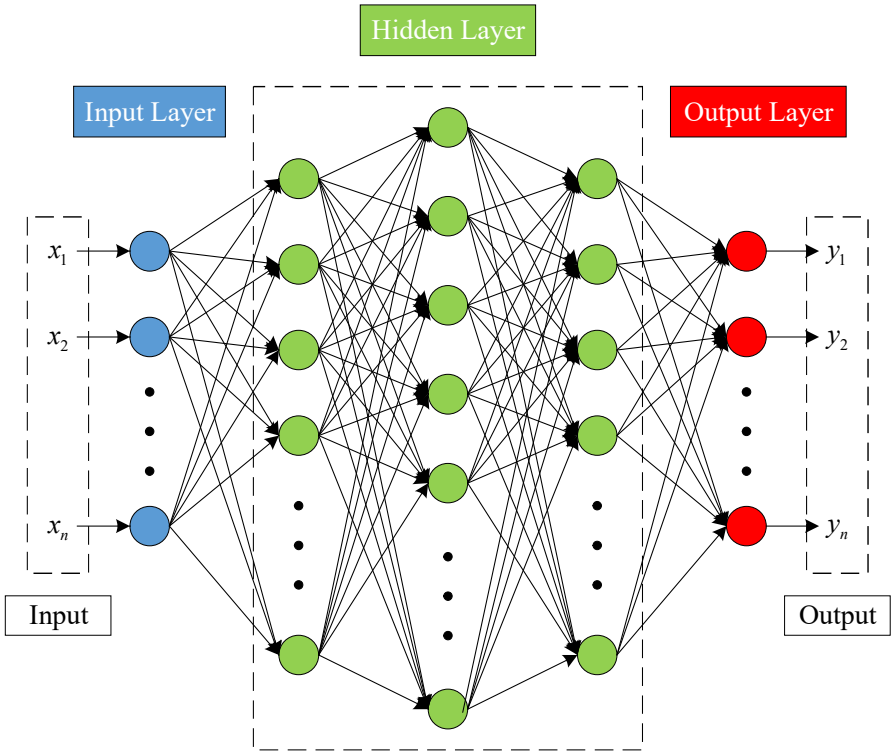

Figure 8. DNN architecture.

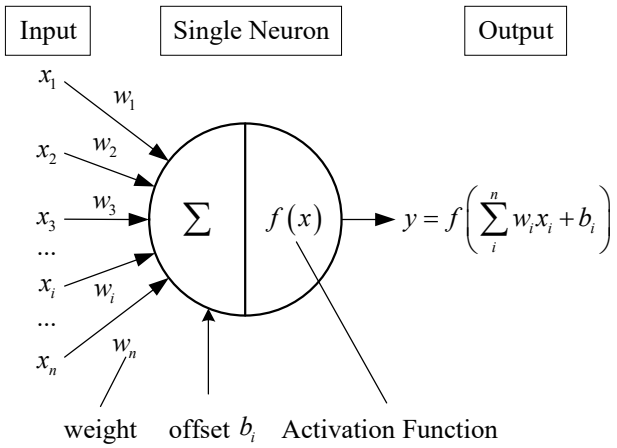

Figure 9. Single-neuron model.

The construction of a deep neural network (DNN) agent model typically involves two stages: forward propagation and backward propagation. During the forward propagation stage, the distance from the input layer to the output layer is computed using training samples in order to estimate the output result of the test samples. Subsequently, network parameters are adjusted to minimize the discrepancy between the calculated outputs for training samples and their target values. In the backward propagation stage, the gradient descent algorithm is employed to optimize the loss function and determine weight matrices and bias terms that yield minimal loss values as optimal parameters. The mean-squared error function (MSE) serves as the utilized loss function in this study:

$$J(\mathbf{W}, \mathbf{B}, x, y) = \frac{1}{n}\sum_{i=1}^{n} \|y_i - f(x_i)\|^2 \tag{13}$$

In this equation, **W** and **B** represent the input weight matrix and bias matrix, respectively, while y_i and $f(x_i)$ represent the theoretical value and predicted value of the output of layer i, respectively. $\|\bullet\|$ represents the Euclidean norm. For each layer, **W** and **B** satisfy the following relationship:

$$f(x_i) = \sigma(z_i) = \sigma(\mathbf{W}_i f(x_{i-1}) + \mathbf{B}_i) \tag{14}$$

where z_i is the input of layer i, and $\sigma(\bullet)$ is the activation function, which is adopted as the ReLU activation function, whose nonlinear ability can make the DNN perform better in nonlinear regression, not only accelerating the convergence speed but also improving the model's predictive ability. Then, the loss function in Equation (13) can be rewritten as follows:

$$J(\mathbf{W}, \mathbf{B}, x, y) = \frac{1}{n}\sum_{i=1}^{n} \|y_i - \sigma(\mathbf{W}_i f(x_{i-1}) + \mathbf{B}_i)\|^2 \tag{15}$$

From the above equation, we can obtain the gradients of **W** and **B** as follows:

$$\frac{\partial J(\mathbf{W}, \mathbf{B}, x, y)}{\partial \mathbf{W}_i} = [(y_i - f(x_i)) \odot \sigma(z_i)][f(x_{i-1})]^{\mathbf{T}} \tag{16}$$

$$\frac{\partial J(\mathbf{W}, \mathbf{B}, x, y)}{\partial \mathbf{B}_i} = (y_i - f(x_i)) \odot \sigma(z_i) \tag{17}$$

Then, the gradient for any layer j is as follows:

$$\delta_j = \frac{\partial J(\mathbf{W}, \mathbf{B}, x, y)}{\partial z_j} = \left(\frac{\partial z_i}{\partial z_{i-1}} \bullet \frac{\partial z_{i-1}}{\partial z_{i-2}} \cdots \bullet \frac{\partial z_{j+1}}{\partial z_j}\right) \frac{\partial J(\mathbf{W}, \mathbf{B}, x, y)}{\partial z_i} \tag{18}$$

According to the forward propagation algorithm, $\mathbf{W}_j$ and $\mathbf{B}_j$ satisfy the following relationship:

$$z_j = \mathbf{W}_j f(x_{j-1}) + \mathbf{B}_j \tag{19}$$

Then, the gradients of $\mathbf{W}_j$ and $\mathbf{B}_j$ in layer j are as follows:

$$\frac{\partial J(\mathbf{W}, \mathbf{B}, x, y)}{\partial \mathbf{W}_j} = \delta_j \left[f(x_{j-1}) \right]^{\mathbf{T}} \tag{20}$$

$$\frac{\partial J(\mathbf{W}, \mathbf{B}, x, y)}{\partial \mathbf{B}_j} = \delta_j \tag{21}$$

From the recursive formula above, we can derive the following:

$$\delta_j = \left(\mathbf{W}_{j+1} \right)^{\mathbf{T}} \delta_{j+1} \odot \sigma(z_j) \tag{22}$$

If the hidden layer j contains m neurons, then the updates for $\mathbf{W}_j$ and $\mathbf{B}_j$ of layer j are represented as follows:

$$\mathbf{W}_j = \mathbf{W}_j - \alpha \sum_{p=1}^{m} \delta_{p,j} \left[f(x_{p,j-1}) \right]^{\mathbf{T}} \tag{23}$$

$$\mathbf{B}_j = \mathbf{B}_j - \alpha \sum_{p=1}^{m} \delta_{p,j} \tag{24}$$

In this formula, α represents the learning efficiency.

During the forward propagation process of constructing a DNN, the weights and biases of each layer's neuron nodes are initialized randomly, resulting in a stochastic prediction, $f(x_i)$. Subsequently, employing the backpropagation algorithm, the neural network parameters undergo fine-tuning based on the loss function, Equation (13), to progressively converge towards their theoretical values. After multiple iterations of weight and bias updates, the trained DNN surrogate model is obtained.

3.2. Construction of Proxy Model for Coordination Mechanism Based on DNN

According to the construction method of the DNN surrogate model, training samples for training the DNN surrogate model are first obtained, and multiple values are extracted and combined in the subintervals of each uncertain input parameter interval to form the input samples for training the DNN surrogate model. The input samples are taken into the coordination mechanism dynamics model for solving to obtain corresponding output responses to form the training set, validation set, and test set of the surrogate model, and then the input samples and output responses are used for training the DNN surrogate model. Among them, 1000 groups of input samples are selected, and the sampling intervals of uncertain input parameters of the input samples are shown in Table 1.

Table 1. Input parameter training set sampling interval.

Symbol	Uncertain Parameters	Value Range	Theoretical Design Value
M_{XT}	Loading (without drug) mass of drug-coordinating arm/kg	[101.14, 105.73]	102.06
m_y	Module drug weight (6 blocks)/kg	[20.2, 20.4]	20.24
R_1	Upper cylinder fulcrum pin radius/mm	[12.4, 12.5]	12.5
R_2	Upper cylinder fulcrum hole radius/mm	[12.5, 12.6]	12.5
R_3	Radius of coordinator fulcrum hole/mm	[12.5, 12.6]	12.5
R_4	Lower fulcrum shaft radius of cylinder/mm	[14.9, 15]	15
R_5	Lower fulcrum hole radius of cylinder/mm	[15, 15.1]	15
μ	Coefficient of friction	[0.25, 0.35]	0.3

The regression performance of the coordinating agency DNN surrogate model on the training set, validation set, and test set is shown in Figure 10. As can be seen from the training results, the complex correlation coefficients, R, of the training set, validation set, and test set are all above 0.9, indicating the accuracy and effectiveness of the trained coordinating agency DNN surrogate model, which can be used for subsequent uncertainty analysis and interval parameter optimization.

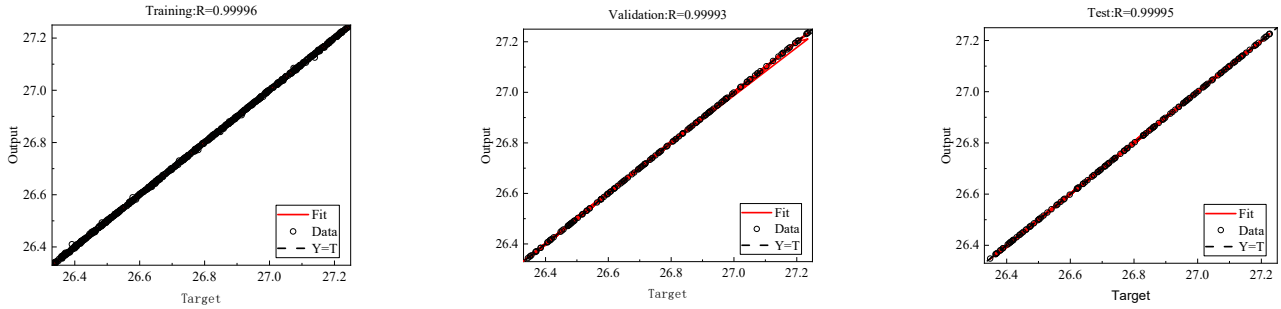

Figure 10. Performance of DNN proxy model for coordination agencies.

4. Uncertainty Propagation Analysis Method Based on Subinterval Prediction

In this section, a subinterval prediction-based uncertainty propagation analysis method is proposed and applied to the uncertainty analysis of the coordinating mechanism. This method can accurately predict the upper and lower boundaries of the uncertainty output, providing a theoretical basis for subsequent parameter optimization.

4.1. Directional Subinterval Prediction Method

Taking the two-dimensional uncertain input vector, $\mathbf{X} = (X_1, X_2)$, interval analysis problem as an example, for convenience, assume that both input parameter intervals are divided into m subintervals and stipulate that m is 2^j, where j is a non-negative integer. One of the difficulties of the classical subinterval prediction method is that it needs to perform a first-order Taylor approximation on all the subinterval combinations, and in the two-dimensional problem, it needs to perform a first-order Taylor approximation on the midpoint of all the subinterval combinations. To solve this problem, this paper proposes a directional subinterval prediction method, which can reduce the number of points to be calculated. Firstly, select any subinterval, $\mathbf{X}_0^I$, in the subinterval domain of the input vector $\mathbf{X}$, and according to the classical subinterval prediction method, conduct a first-order Taylor expansion at the midpoint, $\mathbf{X}_0^c$, of the subinterval with an amplitude of $\Delta\mathbf{X}/m$:

$$f\left(\mathbf{X}_0^I\right) = f(\mathbf{X}_0^c) + \frac{\partial f(\mathbf{X})}{\partial \mathbf{X}}\Big|_{\mathbf{X}=\mathbf{X}_0^c} \frac{\Delta \mathbf{X}}{m}, \tag{25}$$

where $\mathbf{X}_0^I = [\mathbf{X}_0^c - \mathbf{X}^r/m, \mathbf{X}_0^c + \mathbf{X}^r/m]$. The upper and lower bounds of $f\left(\mathbf{X}_0^I\right)$ can be expressed as follows:

$$f^l\left(\mathbf{X}_0^I\right) = f(\mathbf{X}_0^c) - \left|\frac{\partial f(\mathbf{X})}{\partial \mathbf{X}}\Big|_{\mathbf{X}=\mathbf{X}_0^c}\right| \frac{\mathbf{X}^r}{m} \tag{26}$$

$$f^u\left(\mathbf{X}_0^I\right) = f(\mathbf{X}_0^c) + \left|\frac{\partial f(\mathbf{X})}{\partial \mathbf{X}}\Big|_{\mathbf{X}=\mathbf{X}_0^c}\right| \frac{\mathbf{X}^r}{m} \tag{27}$$

To avoid performing first-order Taylor expansions at each central point of the subinterval domain, a reasonable approach is to find an expansion path and predict the upper bound of $f(\mathbf{X})$ by applying first-order Taylor expansions at multiple points on the path. When predicting the upper bound of $f(\mathbf{X})$, the expansion path of extension points should move in the direction of the increasing output response function. Therefore, according to

the gradient of $f(\mathbf{X})$ relative to $\mathbf{X}$ at $\mathbf{X}_0^c$, the next expansion point, $\mathbf{X}_{u1}^c$, required to predict the upper bound can be expressed as follows:

$$\mathbf{X}_{u1}^c = \mathbf{X}_0^c + sign\left(\frac{\partial f(\mathbf{X})}{\partial \mathbf{X}}\Big|_{\mathbf{X}=\mathbf{X}_0^c}\right)\frac{\mathbf{X}^r}{m} \tag{28}$$

The first-order Taylor expansion of $f(\mathbf{X})$ with an amplitude of $\Delta\mathbf{X}/m$ at $\mathbf{X}_{u1}^c$ is as follows:

$$f\left(\mathbf{X}_{u1}^I\right) = f(\mathbf{X}_{u1}^c) + \frac{\partial f(\mathbf{X})}{\partial \mathbf{X}}\Big|_{\mathbf{X}=\mathbf{X}_{u1}^c}\frac{\Delta\mathbf{X}}{m} \tag{29}$$

where the subinterval $\mathbf{X}_{u1}^I = [\mathbf{X}_{u1}^c - \mathbf{X}^r/m, \mathbf{X}_{u1}^c + \mathbf{X}^r/m]$. The upper and lower bounds of $f(\mathbf{X}_{u1})$ obtained from (26) and (27) can be expressed as follows:

$$f^l\left(\mathbf{X}_{u1}^I\right) = f(\mathbf{X}_{u1}^c) - \left|\frac{\partial f(\mathbf{X})}{\partial \mathbf{X}}\Big|_{\mathbf{X}=\mathbf{X}_{u1}^c}\right|\frac{\mathbf{X}^r}{m} \tag{30}$$

$$f^u\left(\mathbf{X}_{u1}^I\right) = f(\mathbf{X}_{u1}^c) + \left|\frac{\partial f(\mathbf{X})}{\partial \mathbf{X}}\Big|_{\mathbf{X}=\mathbf{X}_{u1}^c}\right|\frac{\mathbf{X}^r}{m} \tag{31}$$

When the above steps are performed $n-1$ times in the same way, all the expansion points, $\mathbf{X}_{ui}^c$, used to predict the upper bound can be uniformly expressed by the following equation:

$$\mathbf{X}_{ui}^c = \mathbf{X}_{u(i-1)}^c + sign\left(\frac{\partial f(\mathbf{X})}{\partial \mathbf{X}}\Big|_{\mathbf{X}=\mathbf{X}_{u(i-1)}^c}\right)\frac{\mathbf{X}^r}{m},\ i = 1, 2, \ldots, m-1 \tag{32}$$

At the above point, the output response is a first-order Taylor expansion with an amplitude of $\Delta\mathbf{X}/m$, and the upper and lower bounds of all the expansion points' output responses are obtained as follows:

$$f^l\left(\mathbf{X}_{ui}^I\right) = f(\mathbf{X}_{ui}^c) - \left|\frac{\partial f(\mathbf{X})}{\partial \mathbf{X}}\Big|_{\mathbf{X}=\mathbf{X}_{ui}^c}\right|\frac{\mathbf{X}^r}{m},\ i = 1, 2, \ldots, m-1 \tag{33}$$

$$f^u\left(\mathbf{X}_{ui}^I\right) = f(\mathbf{X}_{ui}^c) + \left|\frac{\partial f(\mathbf{X})}{\partial \mathbf{X}}\Big|_{\mathbf{X}=\mathbf{X}_{ui}^c}\right|\frac{\mathbf{X}^r}{m},\ i = 1, 2, \ldots, m-1 \tag{34}$$

where the subinterval $\mathbf{X}_{ui}^I = [\mathbf{X}_{ui}^c - \mathbf{X}^r/m, \mathbf{X}_{ui}^c + \mathbf{X}^r/m]$, and the upper bound of $f\left(\mathbf{X}_{u1}^I, \mathbf{X}_{u2}^I, \ldots, \mathbf{X}_{ui}^I\right)$ can be obtained by interval fusion:

$$f^u\left(\mathbf{X}_{u1}^I, \mathbf{X}_{u2}^I, \ldots, \mathbf{X}_{ui}^I\right) = \underset{i=1,2,\ldots,m-1}{\cup} f^u\left(\mathbf{X}_{ui}^I\right) = \max_{i=1,2,\ldots,m-1} f^u\left(\mathbf{X}_{ui}^I\right) \tag{35}$$

Similar to the method used for calculating the upper bound of the output response value interval, when predicting the lower bound of $f(\mathbf{X})$, the expansion path of the extension point should move along the direction of the decreasing output response function. Therefore, according to the gradient of $f(\mathbf{X})$ relative to $\mathbf{X}$ at $\mathbf{X}_0^c$, all the expansion points, $\mathbf{X}_{li}^c$, required for predicting the lower bound can be uniformly expressed as follows:

$$\mathbf{X}_{li}^c = \mathbf{X}_{l(i-1)}^c - sign\left(\frac{\partial f(\mathbf{X})}{\partial \mathbf{X}}\Big|_{\mathbf{X}=\mathbf{X}_{l(i-1)}^c}\right)\frac{\mathbf{X}^r}{m},\ i = 1, 2, \ldots, m-1 \tag{36}$$

According to (33) and (34), the upper and lower bounds of the output responses of all the expansion points are as follows:

$$f^l\left(\mathbf{X}_{li}^I\right) = f(\mathbf{X}_{li}^c) - \left|\frac{\partial f(\mathbf{X})}{\partial \mathbf{X}}\Big|_{\mathbf{X}=\mathbf{X}_{li}^c}\right|\frac{\mathbf{X}^r}{m},\ i = 1, 2, \ldots, m-1 \tag{37}$$

$$f^u\left(\mathbf{X}_{li}^I\right) = f(\mathbf{X}_{li}^c) + \left|\frac{\partial f(\mathbf{X})}{\partial \mathbf{X}}\Big|_{\mathbf{X}=\mathbf{X}_{li}^c}\right|\frac{\mathbf{X}^r}{m},\ i = 1, 2, \ldots, m-1 \tag{38}$$

where the subinterval $\mathbf{X}_{li}^{I} = [\mathbf{X}_{li}^{c} - \mathbf{X}^{r}/m, \mathbf{X}_{li}^{c} + \mathbf{X}^{r}/m]$. According to Equation (35), the lower bound of $f\left(\mathbf{X}_{l1}^{I}, \mathbf{X}_{l2}^{I}, \ldots, \mathbf{X}_{li}^{I}\right)$ can be obtained by interval fusion:

$$f^{l}\left(\mathbf{X}_{l1}^{I}, \mathbf{X}_{l2}^{I}, \ldots, \mathbf{X}_{li}^{I}\right) = \underset{i=1,2,\ldots,m-1}{\cup} f^{l}\left(\mathbf{X}_{li}^{I}\right) = \min_{i=1,2,\ldots,m-1} f^{l}\left(\mathbf{X}_{li}^{I}\right) \tag{39}$$

The directional subinterval prediction is based on gradient analysis by constructing two expansion paths from $\mathbf{X}_0$ to $\mathbf{X}_{ui}^{c}$ and $\mathbf{X}_{li}^{c}$ and selecting two subinterval sets along different expansion paths. Therefore, when predicting the response interval, only a small number of points on the paths with increasing or decreasing gradients are selected for the first-order Taylor expansion. Compared with the classical subinterval analysis method, this method can greatly reduce the amount of calculation needed. In order to simplify the analysis process, in the above description of the two-dimensional problem, each input parameter is divided into the same number of subintervals, while different input parameters can be set to different numbers of subintervals according to the needs of the actual problem.

4.2. Adaptive Strategy for Subinterval Partitioning

In the subinterval prediction analysis method, the accuracy of the prediction results is closely related to the number of subintervals. When the input parameter interval is divided into a sufficient number of subintervals, both classical subinterval prediction and improved directional subinterval prediction can achieve sufficient accuracy. However, an increase in the number of subintervals means an increase in the number of calculations and a decrease in calculation efficiency. Therefore, on the premise of ensuring accuracy, it is an important measure to reduce the number of subintervals divided by the input parameter interval as much as possible to improve the calculation efficiency.

According to the directional subinterval prediction method in the previous section, the output response is first expanded by the first-order Taylor series at the midpoint of the input parameter interval, and the upper and lower bounds of the initial interval, $f_0^{l}\left(\mathbf{X}^{I}\right)$ and $f_0^{u}\left(\mathbf{X}^{I}\right)$, can be obtained by Equations (30) and (31). If the initial interval cannot meet the prediction accuracy of the output response, a subinterval division of the input parameter interval is needed. Therefore, after obtaining the initial interval, $f(\mathbf{X})$, the parameter interval is divided into two equal subintervals by the midpoint of the interval, where the first-order Taylor series is first expanded. Then, the first-order Taylor series is, respectively, expanded at the midpoints of the two subintervals, and the new upper and lower bounds of the interval $f(\mathbf{X})$ can be obtained by Equations (35) and (39). The adaptive strategy for subinterval division is shown in Figure 11 below.

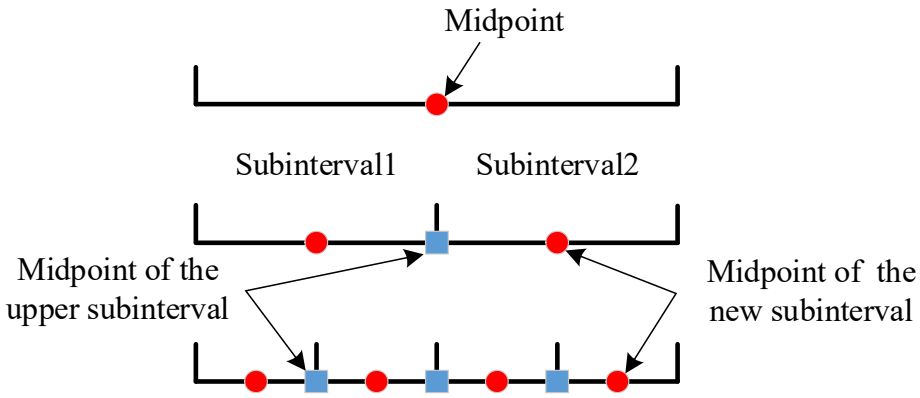

Figure 11. Schematic diagram of adaptive strategy for subinterval partition.

Global convergence is guaranteed on the premise of ensuring accuracy. The convergence index is defined as follows:

$$\begin{matrix} \left| \frac{f_q^u(\mathbf{X}^I) - f_{q-1}^u(\mathbf{X}^I)}{f_q^u(\mathbf{X}^I)} \right| \le \varepsilon_1 \\ \left| \frac{f_q^l(\mathbf{X}^I) - f_{q-1}^l(\mathbf{X}^I)}{f_q^l(\mathbf{X}^I)} \right| \le \varepsilon_2 \end{matrix}, \tag{40}$$

where q is the number of adaptive iterations for subinterval division; $f_q^l\left(\mathbf{X}^I\right)$ and $f_q^u\left(\mathbf{X}^I\right)$ are the upper and lower bounds of the output response value interval calculated from q iterations; $f_{q-1}^l\left(\mathbf{X}^I\right)$ and $f_{q-1}^u\left(\mathbf{X}^I\right)$ are the upper and lower bounds calculated through $(q-1)$ iterations; and ε_1 and ε_2 are the defined convergence indexes, namely, the accuracy indexes representing the output response prediction.

4.3. Computing Process

To sum up, the main flow chart of the directional subinterval prediction method is shown in Figure 12, and the specific implementation steps are as follows:

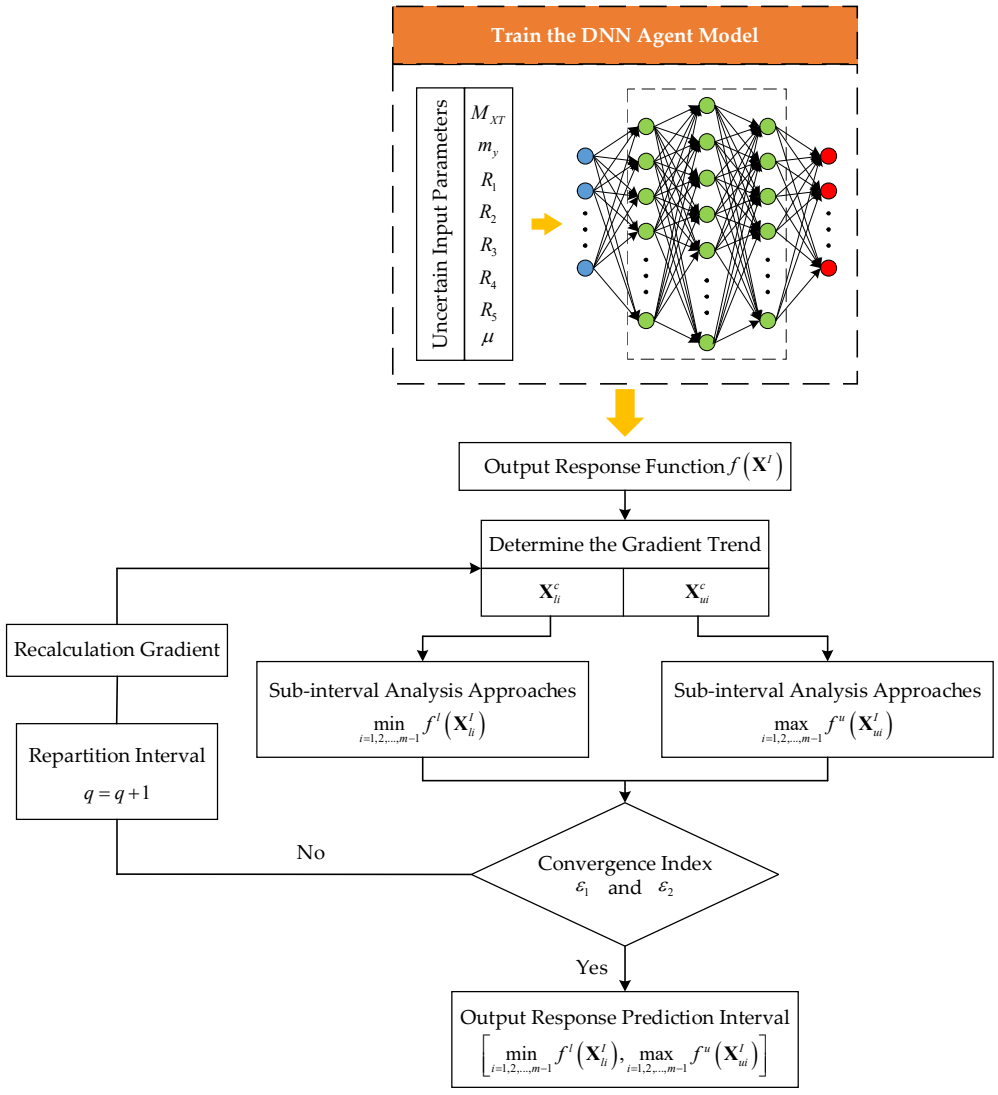

Figure 12. Main flow chart of directional subinterval prediction method.

Step 1: Summarize the main influencing factors according to the mechanism failure mode, list the uncertain input parameters, and determine the uncertain input parameters by referring to the previous structural design, specified indicators, and existing experimental data.

Step 2: Determine the uncertain output response according to the mechanism's uncertainty problem and construct the output response function, $f\left(\mathbf{X}^I\right)$. Let $q = 0$.

Step 3: Find the appropriate expansion path for predicting the upper and lower bounds of the output response according to the gradient analysis of $f\left(\mathbf{X}^I\right)$.

Step 4: Calculate the upper and lower bounds of the value interval of $f\left(\mathbf{X}_{ui}^I\right)$ and $f\left(\mathbf{X}_{li}^I\right)$, respectively, according to Equations (33) and (34) and Equations (37) and (38). Predict the upper and lower bounds of the interval $f\left(\mathbf{X}^I\right)$ according to Equations (35) and (39) through interval fusion.

Step 5: Test whether the upper and lower bounds of $f\left(\mathbf{X}^I\right)$ obtained through the q iterations meet the specified convergence index. If they do meet it, the output response prediction interval is obtained; if not, proceed to Step 6.

Step 6: Divide the value interval of the input parameters into two equal subintervals with the midpoint of the interval as the dividing line, take the midpoints of the two new subintervals as the expansion point, and return to Step 3, with $q = q + 1$.

5. Analysis of Uncertainty Propagation in Coordination Mechanism Based on Subinterval Prediction

Based on the DNN surrogate model of the coordinating mechanism established in the previous section, the uncertainty of the positioning accuracy of the coordinating mechanism is quantitatively analyzed by using the directional subinterval prediction method and the subinterval division and convergence strategy. According to the theoretical design and engineering practice of the coordinating mechanism, the value interval and uncertainty level of the uncertainty input parameters of the coordinating mechanism are shown in Table 2.

Table 2. Uncertainty input parameter interval and uncertainty level.

Index	Uncertain Parameters	Value Range	Theoretical Design Value
1	Loading (without drug) mass of drug-coordinating arm/kg	[101.14, 105.73]	0.0222
2	Module drug weight (6 blocks)/kg	[20.2, 20.4]	0.0049
3	Upper cylinder fulcrum pin radius/mm	[12.4, 12.5]	0.004
4	Upper cylinder fulcrum hole radius/mm	[12.5, 12.6]	0.004
5	Radius of coordinator fulcrum hole/mm	[12.5, 12.6]	0.004
6	Lower fulcrum shaft radius of cylinder/mm	[14.9, 15]	0.0033
7	Lower fulcrum hole radius of cylinder/mm	[15, 15.1]	0.0033
8	Coefficient of friction	[0.25, 0.35]	0.1667

The uncertain input parameter interval is brought into the DNN surrogate model of the coordinating mechanism, and the directional subinterval prediction method is used to calculate the interval boundary of the output response of the coordinating mechanism, where the convergence index is set to $\varepsilon_1 = \varepsilon_2 = 0.01$. In addition, in order to determine the accuracy of the proposed method, the results of the MCS method are used as the accurate solution, where the number of iterations in the MCS method is 10^6, and the results of the first-order Taylor expansion method and the classical subinterval prediction method are used as the reference solution. The results are shown in Figure 13 and Table 3.

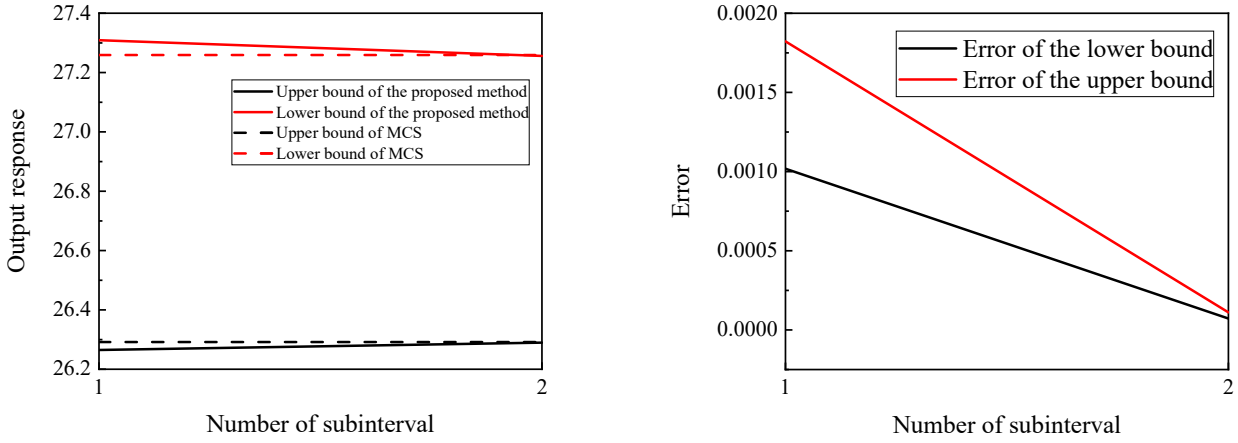

(**a**) Output response boundary contrast (**b**) Error contrast

Figure 13. Output response boundary and error comparison of coordination mechanisms obtained by directional subinterval prediction method and MCS method.

Table 3. Upper and lower boundaries of output responses of coordination mechanisms obtained by different analytical methods.

Methods	Lower Bound of Output Response		Upper Bound of Output Response		Number of Calls
	Value	Error	Value	Error	
MCS	26.2917	—	27.2592	—	10^6
First-order Taylor expansion	26.2649	10.19‰	27.3089	18.23‰	9
Classical subinterval prediction	26.2737	6.85‰	27.2749	5.76‰	2304
Directional subinterval prediction	26.2898	0.72‰	27.2562	1.10‰	27

The output response boundary results of the coordinating mechanisms using the directional subinterval prediction are shown in Figure 13a. As can be seen from the figure, the convergence results of the output response boundary are obtained only through two adaptive iterations, in which each uncertain input parameter interval is divided into two subintervals. The upper and lower boundaries of the output response of the coordinating mechanism are very close to the exact solution calculated by the MCS method, with relative errors of only 0.72‰ and 1.10‰, and the accuracy can be improved again by increasing the number of subintervals. The results of the first-order Taylor expansion method and the classical subinterval prediction method are shown in Table 3. From the table, the relative errors of the lower boundary of the output response obtained by the first-order Taylor expansion method and the classical subinterval prediction method are 10.19‰ and 6.85‰, respectively. The results of the directional subinterval prediction method and the classical subinterval prediction method are in good agreement with the exact solution. However, the directional subinterval prediction method only needs 27 iterations of the surrogate model, while the classical subinterval prediction method needs a subinterval analysis of all the possible subinterval combinations, so it needs 2304 iterations. Therefore, the directional subinterval prediction method proposed in this paper can greatly reduce the calculation cost and improve the calculation efficiency under the premise of ensuring accuracy, indicating that this method can be used in uncertainty analysis and follow-up research on coordinating mechanisms.

6. Conclusions

This paper investigates the coordination mechanism of a cartridge conveying system by constructing a rigid–flexible coupling dynamics model of the coordination mechanism with a hinged gap, based on models of shaft–hole hinged gaps and flexible cantilever

beams. Through conducting experiments on the principle prototype platform and analyzing recorded data, we compare the output response under actual conditions with that obtained from simulation using the dynamics model to verify its accuracy and effectiveness. However, due to the numerous calculation models required in uncertainty analysis, employing a high-precision dynamics model would result in significant computational costs. Therefore, we utilize a deep neural network surrogate model as an alternative for the simulation calculations instead. Subsequently, we propose a directional subinterval prediction method based on classical subinterval prediction methods and employ an adaptive subinterval partition method to accurately approximate output response interval boundaries while reducing the use of the model. This approach is then applied to predict the positioning accuracy of the coordination mechanism under uncertain input parameters, obtaining an output response interval influenced by these uncertainties. The results are compared with those obtained from Monte Carlo simulations (MCS), the first-order Taylor expansion method, and classical subinterval prediction methods. Our findings demonstrate close agreement between the outcomes derived from our proposed method and the exact solutions derived from the MCS simulations. Moreover, compared to a MCS, which requires 10^6 function calls in order to obtain results, only 27 function calls are needed when using our proposed method. In contrast to conventional analysis methods like MCSs, not only does our proposed method exhibit higher accuracy, but it also demonstrates superior efficiency.

Author Contributions: Writing—original draft, X.G.; Writing—review & editing, L.C. and J.T. All authors have read and agreed to the published version of the manuscript.

Funding: This research received no external funding.

Data Availability Statement: The data presented in this study are available on request from the corresponding author. The data are not publicly available due to privacy.

Conflicts of Interest: The authors declare no conflict of interest.

References

1. Zhou, K.; Wang, Z.; Gao, Q.; Yuan, S.; Tang, J. Recent advances in uncertainty quantification in structural response characterization and system identification. *Probabilistic Eng. Mech.* **2023**, *74*, 103507. [CrossRef]
2. Elishakoff, I.; Ren, Y. The bird's eye view on finite element method for structures with large stochastic variations. *Comput. Methods Appl. Mech. Eng.* **1999**, *168*, 51–61. [CrossRef]
3. Ye, N.; Lu, Z. Single-loop cross-entropy-based directional importance sampling for efficient estimation of failure probability function. *Aerosp. Sci. Technol.* **2024**, *146*, 108962. [CrossRef]
4. Ting, Y.; Zhenzhou, L. A novel single-loop Kriging importance sampling method for estimating failure probability upper bound under random-interval mixed uncertainties. *Aerosp. Sci. Technol.* **2023**, *143*, 108722.
5. Liao, Z.; Xia, W.; He, X. An investigation into Markov chain Monte Carlo algorithms for Subset simulation: Emphasizing uncertainty analysis. *Comput. Struct.* **2024**, *294*, 107268. [CrossRef]
6. Prabhu, S.; Ehrett, C.; Javanbarg, M.; Brown, D.A.; Lehmann, M.; Atamturktur, S. Uncertainty Quantification in Fault Tree Analysis: Estimating Business Interruption due to Seismic Hazard. *Nat. Hazards Rev.* **2020**, *21*, 04020015. [CrossRef]
7. Saberi, S.; Abdollahi, A.; Friswell, M.I. Probability analysis of bistable composite laminates using the subset simulation method. *Compos. Struct.* **2021**, *271*, 114120. [CrossRef]
8. Poikonen, T.; Blattner, P.; Kärhä, P.; Ikonen, E. Uncertainty analysis of photometer directional response index f SUB2/SUB using Monte Carlo simulation. *Metrologia* **2012**, *49*, 727–736. [CrossRef]
9. Ben-Haim, Y.; Elishakoff, I. *Convex Models of Uncertainty in Applied Mechanics*; Elsevier: Amsterdam, The Netherlands, 2013.
10. Zhou, Y.; Huang, G.; Wang, S.; Zhai, Y.; Xin, X. Water resources management under dual uncertainties: A factorial fuzzy two-stage stochastic programming approach. *Stoch. Environ. Res. Risk Assess.* **2016**, *30*, 795–811. [CrossRef]
11. Qiu, Z.; Lv, Z. The vertex solution theorem and its coupled framework for static analysis of structures with interval parameters. *Int. J. Numer. Methods Eng.* **2017**, *112*, 711–736. [CrossRef]
12. Ma, Y.; Liang, Z.; Chen, M.; Hong, J. Interval analysis of rotor dynamic response with uncertain parameters. *J. Sound Vib.* **2013**, *332*, 3869–3880. [CrossRef]
13. Liu, Y.S.; Wang, X.J.; Wang, L. Interval uncertainty analysis for static response of structures using radial basis functions. *Appl. Math. Model.* **2019**, *69*, 425–440. [CrossRef]
14. Liu, Y.S.; Wang, X.J.; Wang, L.; Zheng, L. A Bayesian collocation method for static analysis of structures with unknown-but-bounded uncertainties. *Comput. Methods Appl. Mech. Eng.* **2019**, *346*, 727–745. [CrossRef]

15. Wang, L.; Chen, Z.; Yang, G. An interval uncertainty analysis method for structural response bounds using feedforward neural network differentiation. *Appl. Math. Model.* **2020**, *82*, 449–468. [CrossRef]
16. Wei, T.H.; Meng, G.W.; Li, F.; Cong, Y.B. Interval analysis of structure based on dimension reduction method and Chebyshev polynomial. *Huazhong Univ. Sci. Technol. (Nat. Sci. Ed.)* **2021**, *41*, 14–19.
17. Chen, S.H.; Lian, H.D.; Yang, X.W. Interval static displacement analysis for structures with interval parameters. *Int. J. Numer. Methods Eng.* **2002**, *53*, 393–407. [CrossRef]
18. Ma, K.; Li, B.H.; Yang, K.; Liu, Q.L. First and second-order sensitivity method of structure static displacement. *J. Jilin Univ. (Eng. Technol. Ed.)* **2021**, *51*, 472–477.
19. Li, J.P.; Chen, J.J.; Zhu, Z.Q.; Li, J.P.; Chen, J.J.; Zhu, Z.Q. A Method for Solving the Structural Interval Finite Element Equations. *Eng. Mech.* **2010**, *27*, 79–83.
20. Wu, P.G.; Ni, B.Y.; Jiang, C. An Interval Finite Element Method Based on the Neumann Series Expansion. *Chin. J. Theor. Appl. Mech.* **2020**, *52*, 1431–1442.
21. Qiu, Z.; Elishakoff, I. Antioptimization of structures with large uncertain-but-non-random arameters via interval analysis. *Comput. Methods Appl. Mech. Eng.* **1998**, *152*, 361–372. [CrossRef]
22. Zhou, Y.T.; Jiang, C.; Han, X. Interval and subinterval analysis methods of the structural analysis and their error estimations. *Int. J. Comput. Methods* **2006**, *3*, 229–244. [CrossRef]
23. Chen, N.; Yu, D.; Xia, B.; Liu, J.; Ma, Z. Interval and subinterval homogenization-based method for determining the effective elastic roperties of periodic microstructure with interval parameters. *Int. J. Solids Struct.* **2017**, *106–107*, 174–182. [CrossRef]
24. Fu, C.M.; Cao, L.X.; Tang, J.C.; Long, X.Y. A subinterval decomposition analysis method for uncertain structures with large uncertainty parameters. *Comput. Struct.* **2018**, *197*, 58–69. [CrossRef]
25. Aloisio, A.; Contento, A.; Alaggio, R.; Quaranta, G. Physics-based models, surrogate models and experimental assessment of the vehicle–bridge interaction in braking conditions. *Mech. Syst. Signal Process.* **2023**, *194*, 110276. [CrossRef]
26. Cunha, B.Z.; Droz, C.; Zine, A.M.; Foulard, S.; Ichchou, M. A review of machine learning methods applied to structural dynamics and vibroacoustic. *Mech. Syst. Signal Process.* **2023**, *200*, 110535. [CrossRef]
27. Chen, Z.Q.; Qian, L.F.; Chen, G.S.; Nie, S.C.; Yin, Q. Dynamics of luffing motion of a hydraulically driven shell manipulator with revolute clearance joints. *Def. Technol.* **2022**, *18*, 689–708.